# Near-Field Nonuniformities in Angularly-Multiplexed KrF Fusion Lasers with Induced Spatial Incoherence

R. H. Lehmberg and Y. Chan

*Plasma Physics Division, U. S. Naval Research Laboratory*

*Washington, DC 20375, USA*

*Tel: (202) 404-4441; Fax: (202) 767-0046; E-mail: lehmberg@this.nrl.navy.mil*

## Abstract

Induced Spatial Incoherence (ISI) has been proposed for KrF laser drivers to achieve the high degree of spatial beam uniformity required for direct-drive inertial confinement fusion. Although ISI provides ultrasmooth illumination at the far-field of the laser, where the target is located, it can still allow the beams in the quasi near-field to develop time-averaged spatial structure. This speckle, which arises primarily from random phase aberration, builds up as the laser beams propagate away from the pupil plane located at the final amplifier stage; it is distinct from any structure imposed by gain nonuniformities in the amplifiers. Because of the spatial incoherence, the speckle is significantly smaller than that experienced by coherent beams; nevertheless, it remains a damage issue, especially for the long beam delay paths required in angularly-multiplexed KrF lasers. This paper develops a novel algorithm for calculating the time-integrated intensities, compares simulations and measurements of the near-field speckle in the Nike KrF laser, and explores options, such as aberration reduction and optical relaying, for controlling the problem in future angularly-multiplexed KrF drivers.

OCIS numbers: 030.6140, 030.6600, 070.2590, 140.2180, 350.2660, 350.5500

*Keywords*: Beam Smoothing; KrF Lasers; Partial Coherence; Near-field; Speckle; FFT

# Report Documentation Page

| 1. REPORT DATE **2005** | 2. REPORT TYPE | 3. DATES COVERED **00-00-2005 to 00-00-2005** |
|---|---|---|

| 4. TITLE AND SUBTITLE | 5a. CONTRACT NUMBER |
|---|---|
| **Near-Field Nonuniformities in Angularly-Multiplexed KrF Fusion Lasers with Induced Spatial Incoherence** | 5b. GRANT NUMBER |
| | 5c. PROGRAM ELEMENT NUMBER |
| 6. AUTHOR(S) | 5d. PROJECT NUMBER |
| | 5e. TASK NUMBER |
| | 5f. WORK UNIT NUMBER |

| 7. PERFORMING ORGANIZATION NAME(S) AND ADDRESS(ES) **Naval Research Laboratory,Plasma Physics Division,4555 Overlook Avenue SW,Washington,DC,20375** | 8. PERFORMING ORGANIZATION REPORT NUMBER |
|---|---|

| 9. SPONSORING/MONITORING AGENCY NAME(S) AND ADDRESS(ES) | 10. SPONSOR/MONITOR'S ACRONYM(S) |
|---|---|
| | 11. SPONSOR/MONITOR'S REPORT NUMBER(S) |

14. ABSTRACT
**Induced Spatial Incoherence (ISI) has been proposed for KrF laser drivers to achieve the high degree of spatial beam uniformity required for direct-drive inertial confinement fusion. Although ISI provides ultrasmooth illumination at the far-field of the laser, where the target is located, it can still allow the beams in the quasi near-field to develop time-averaged spatial structure. This speckle, which arises primarily from random phase aberration, builds up as the laser beams propagate away from the pupil plane located at the final amplifier stage; it is distinct from any structure imposed by gain nonuniformities in the amplifiers. Because of the spatial incoherence, the speckle is significantly smaller than that experienced by coherent beams; nevertheless, it remains a damage issue, especially for the long beam delay paths required in angularly-multiplexed KrF lasers. This paper develops a novel algorithm for calculating the time-integrated intensities, compares simulations and measurements of the near-field speckle in the Nike KrF laser, and explores options, such as aberration reduction and optical relaying, for controlling the problem in future angularly-multiplexed KrF drivers.**

| 15. SUBJECT TERMS | | | | | |
|---|---|---|---|---|---|

| 16. SECURITY CLASSIFICATION OF: | | | 17. LIMITATION OF ABSTRACT | 18. NUMBER OF PAGES | 19a. NAME OF RESPONSIBLE PERSON |
|---|---|---|---|---|---|
| a. REPORT **unclassified** | b. ABSTRACT **unclassified** | c. THIS PAGE **unclassified** | **Same as Report (SAR)** | **38** | |

One of the key requirements for inertial confinement fusion (ICF) is a highly uniform implosion of the spherical target. In direct-drive ICF, this requires the spatial profile of the focused laser beam to be as smooth and controllable as possible. This is especially true early in the pulse when the target has not yet developed the large blowoff plasma that helps smooth the spatial structure by thermal diffusion. Irradiation nonuniformities at these early times can imprint themselves directly onto the target, thereby seeding the Rayleigh-Taylor instability during the acceleration phase. [1],[2] A rapid and effective beam smoothing technique is thus required if the laser facility is to be useful for direct-drive ICF.

Induced spatial incoherence (ISI) is a highly effective technique for achieving the required ultrasmooth illumination with a KrF laser driver.[3]-[10] The Nike KrF laser has produced smooth, nearly flat ISI focal fluences with total speckle nonuniformities (including *all* spatial modes) of 1% rms in a single 4 ns beam[10] and as low as 0.15%-0.2% when multiple angularly-multiplexed beams are overlapped [8]. Using broadband temporally and spatially incoherent light, ISI creates the desired spatial profile at an object aperture in the laser front end, then images it through the laser system onto the target located at the focal spot. The instantaneous intensity is highly nonuniform speckle, but this averages out to the desired profile when averaged over time intervals $t_{av}$ much longer than the laser coherence time $\tau_c \sim 1/\text{bandwidth}$.[3],[11] The time-averaged profile remains smooth and insensitive to laser phase aberration if its angular width is many times diffraction limit and large compared to the point-spread distribution created by that aberration.[6],[7],[8]

Although ISI provides ultrasmooth focal spot illumination, it still allows significant time-

averaged speckle structure to develop in the quasi near-field of the laser. This structure, which builds up the beams propagate away from the pupil-plane images at the amplifiers, arises primarily from upstream random phase aberration; it is distinct from the generally long scalelength variations due to residual gain nonuniformities across the amplifier apertures.[12] In angularly-multiplexed KrF systems, it develops primarily in the long delay path optics (e.g., demultiplexing mirrors and focusing lenses) after the final amplifier. The speckle nonuniformities of ISI beams are much smaller than those created by coherent light, and so far they have not caused any serious damage in the Nike output optics because the average fluences (typically less than 0.5 J/cm$^2$) are well below damage threshold. Nevertheless, they remain a potential damage issue for future KrF driver designs, where the pathlengths and beam sizes would be similar, but the average fluences would have to be higher.[13] A fast and reliable algorithm is therefore needed to simulate and minimize the near-field speckle problem in these future designs. In this paper, we derive such an algorithm, compare its simulations with measurements on the Nike laser, and use it to explore options for controlling the problem in future angularly-multiplexed systems.

We examine two techniques for calculating the average intensities. The first models the instantaneous stochastic optical amplitude at the object-plane by a 2D Gaussian-distributed random complex array, then propagates it through the laser system (whose complex final aperture transmission includes the phase aberration) to evaluate the instantaneous intensity. One then repeats this procedure with multiple new statistical realizations to accumulate the average intensity. The second technique, which is much faster, directly evaluates the average intensity envelope at both the near-field or far-field by using a generalized version of

partially-coherent imaging theory.[11],[14],[15] Starting with the incoherent object envelope, it calculates the optical autocorrelation function before the final amplifier aperture from the Van Cittert-Zernike theorem, then combines it with the phase-aberrated transmission to derive convolution integrals that relate the downstream intensity envelopes to the object. (For the near-field, the point-spread distribution is an aberrated Fresnel diffraction formula.) The convolutions are then evaluated by Fast Fourier Transform (FFT) methods. Benchmark tests show excellent agreement (within $< 1\%$ rms) between the two techniques.

We then compare the theory with calibrated photochromic film images of two Nike laser beams. The simulations assume uniform illumination at the 60 cm final amplifier aperture, a uniformly illuminated circular object aperture of width $75\times$ Diffraction Limit (75 XDL), and random phase aberration of $\sim \lambda/4$ rms amplitude and $\sim 15$ XDL far-field point-spread width. In good qualitative agreement with the measurements, the simulations show that as the distance from the amplifier increases, (a) the structure becomes coarser and (b) the hot-spot amplitudes increase at first, then appear to saturate and slowly decrease. In all cases, the measured and simulated far-field profiles remained smooth.[10]

Finally, we perform additional simulations to explore options for reducing the near-field speckle. One possibility is to reduce the phase aberration; e.g., a two-fold reduction in point-spread width also reduces the intensity variations by $\sim$ two-fold. The second option would reduce the hot-spots by using optical relaying, but that would probably be expensive to implement in some of the longer beam paths required for demultiplexing.

Although this paper addresses only the case of ISI in angularly-multiplexed KrF lasers, the problem of quasi near-field structure is not limited to such systems. Other beam-

smoothing techniques, such as smoothing by spectral dispersion (SSD),[16],[17] optical fiber smoothing (OFS), [18] and partially coherent light (PCL),[19] are also subject to time-integrated near-field structure due to laser phase aberration. These techniques are normally applied to glass lasers, where optical relaying is easier to implement because there are fewer beams; however glass lasers are also more susceptible to small-scale self-focusing, which tends to amplify the near-field nonuniformities.

<center>Theory</center>

Figure 1 illustrates the implementation of ISI in the Nike laser. A spatially and temporally incoherent oscillator uniformly illuminates the object aperture, whose transmission produces the desired time-averaged transverse spatial profile $\langle I_O(\mathbf{x}_O)\rangle = \langle |E_O(\mathbf{x}_O, t)|^2\rangle$ from the rapidly-varying complex speckle amplitudes $E_O(\mathbf{x}_O, t)$. This light is relayed through the laser system, then focused to produce the image $\langle I_F(\mathbf{x}_F)\rangle = \langle |E_F(\mathbf{x}_F, t)|^2\rangle$ at the target. Each amplifier is placed at or near an image of the object's Fourier-transform (FT) plane, where the light from each point of $\langle I_O(\mathbf{x}_O)\rangle$ encodes itself into a bundle of rays that traverse the amplifier at the same unique field angle. Because these angles are small, each bundle is amplified the same and $\langle I_F(\mathbf{x}_F)\rangle$ remains insensitive to laser phase and gain nonuniformities. This insensitivity can also be explained by an alternative picture in which the object profile encodes itself into $N_F^2 \gg 1$ small coherence zones in the FT plane;[4] as long as these zones remain small compared to the nonuniformity scalelengths, they are not strongly affected.

For KrF bandwidths $\Delta\nu \sim 1$ THz and a carrier frequency $\nu_0 = c/\lambda \sim 1200$ THz, we can usually treat the light propagation through the laser system as quasi-monochromatic. This approximation is justified as long as the time-averaged near-field structure arises from

<center>5</center>

interfering rays whose optical path differences are less than the optical coherence length $c\tau_c \simeq c/\Delta\nu \sim 300$ $\mu$m. In the Appendix, we show that this condition is well satisfied in nearly all the simulations presented here because the small transverse width of the spatial coherence zones effectively limits the path differences; the only marginal case is that of spatially coherent (but still finite $\Delta\nu$) light. We will thus simplify the notation by dropping *explicit* references to the time variation of $E_O\left(\mathbf{x}_O, t\right)$ and all other complex amplitudes.

In the Nike laser, the object's FT plane is located at a rectangular entrance pupil aperture of width $D_E$ located a focal distance $f_E$ beyond the input lens. The lens collimates some of the light from the incoherent object to overfill this aperture, which is then imaged into the amplifiers. The instantaneous speckle amplitude is thus[20]

$$E_E\left(\mathbf{x}_E\right) = \left(\lambda f_E\right)^{-1} \mathfrak{F}\left[E_O, -\mathbf{x}_E/\left(\lambda f_E\right)\right] , \tag{1}$$

where $\lambda$ is the optical wavelength and

$$\mathfrak{F}\left(E, \pm\mathbf{x}\right) \equiv \int E\left(\boldsymbol{\xi}\right) \exp\left(\pm i 2\pi \boldsymbol{\xi}\cdot\mathbf{x}\right) d^2\boldsymbol{\xi} \tag{2}$$

defines the 2D spatial FT of $E\left(\boldsymbol{\xi}\right)$. Because of the overfill, we can assume approximately uniform *average* intensity $\left\langle\left|E_E\left(\mathbf{x}_E\right)\right|^2\right\rangle$ within the aperture.

The laser system splits $E_E\left(\mathbf{x}_E\right)$ into numerous angularly-multiplexed beams, then magnifies and image-relays each one through a chain of amplifiers to the final stage, whose aperture $D_A$ acts as the optical stop or exit pupil. In the absence of laser gain and phase aberration, the amplitude just before this aperture would then be $E_A\left(\mathbf{x}_A\right) = E_E\left(\mathbf{x}_A/M_{EA}\right)/M_{EA}$, where $M_{EA}$ is the geometrical optics magnification $M_{EA} \gtrsim D_A/D_E > 1$, and the average intensity $\left\langle\left|E_A\left(\mathbf{x}_A\right)\right|^2\right\rangle$ is again uniform. Because of the amplifier imaging, one can approximately lump

all the laser gain and phase nonuniformities into a single complex aperture transmission

$$T_A\left(\mathbf{x}_A\right) \equiv A\left(\mathbf{x}_A\right)\sqrt{G\left(\mathbf{x}_A\right)}\exp\left[i\phi\left(\mathbf{x}_A\right)\right], \tag{3}$$

where $G\left(\mathbf{x}_A\right)$ is the total power gain, $\phi\left(\mathbf{x}_A\right)$ is the total phase aberration, and $A\left(\mathbf{x}_A\right)$ is the hard aperture transmission. For a square aperture, $A\left(\mathbf{x}_A\right) = 1$ when $|x_A|, |y_A| \leq D_A/2$ and 0 otherwise. The amplitude just beyond the aperture is thus

$$E'_A\left(\mathbf{x}_A\right) \equiv T_A\left(\mathbf{x}_A\right)E_A\left(\mathbf{x}_A\right) = T_A\left(\mathbf{x}_A\right)E_E\left(\mathbf{x}_A/M_{EA}\right)/M_{EA}. \tag{4}$$

The spatial variation of $G\left(\mathbf{x}_A\right)$ includes the effect of gain saturation as well as laser excitation nonuniformity, and is assumed to be only long scalelength. In principle, rapidly-varying speckle could create short scalelength gain nonuniformities due to saturation, but the changes occur so rapidly that the KrF* population is unable to respond.[4] Saturation ensures that the average intensity $\left\langle |E'_A\left(\mathbf{x}_A\right)|^2 \right\rangle$ is similar to the final amplifier excitation profile, which would be approximately uniform in a practical system. The hard aperture diffraction created by $A\left(\mathbf{x}_A\right)$ will cause a slight blurring of the target beam profile $\left\langle I_F\left(\mathbf{x}_F\right)\right\rangle$, but the effect is negligible as long as the width of $\left\langle I_F\left(\mathbf{x}_F\right)\right\rangle$ remains many XDL. In the Nike laser, this profile is typically $\sim 75$ XDL; in a fusion driver it is likely to be even larger.

One can write the complex amplitudes in a compact form suitable for numerical analysis by rescaling transverse near-field coordinates to the geometrical optics beamwidths, the far-field (object and image) coordinates to the diffraction-limited widths, and propagation distances to Fresnel lengths; e.g., $\mathbf{x}_A$ scales to $D_A$, while $\mathbf{x}_O$ scales to $d_O \equiv M_{EA}f_E\lambda/D_A$:

$$\mathbf{X}_A \equiv \mathbf{x}_A/D_A, \quad \mathbf{X}_O \equiv \mathbf{x}_O/d_O. $$

Expressions (1)-(4) then give the amplitude $E'_A(\mathbf{X}_A) = T_A(\mathbf{X}_A) E_A(\mathbf{X}_A)$, where the complex aperture transmission now satisfies $T_A(\mathbf{X}_A) = 0$ for $|X_A|, |Y_A| > \frac{1}{2}$,

$$E_A(\mathbf{X}_A) = F_A \int E_O(\mathbf{X}_O) \exp(-i2\pi\mathbf{X}_A \cdot \mathbf{X}_O) d^2\mathbf{X}_O = F_A \mathfrak{F}(E_O, -\mathbf{X}_A), \tag{5}$$

and $F_A \equiv M_{EA}f_E\lambda/D_A^2 \ll 1$ is an inverse Fresnel number. With these scalings, all near-field beamwidths are limited to $\sim 1$, but the far-field widths can range over many XDL.

Figure 2 shows one of the angularly-multiplexed beams at the output of the optical system. Just after the common aperture stop $A$, a weak focusing optic converges each beam to its collimator mirror $C$ at distance $z_{AC}$. The collimated beam of geometrical optics width $D_C < D_A$ then propagates over a delay distance $z_{CL}$ to the final focusing lens $L$, which is still in the quasi near-field of $A$. The length of the delay path is controlled by the location of demultiplexing mirror $M$, and is different for each beam. In the case of interest, where the beam *underfills* all the optical elements located downstream from $A$, we can calculate its propagation directly from $E'_A(\mathbf{X}_A, t)$. We have assumed that the phase aberration $\phi(\mathbf{X}_A)$ in $T_A(\mathbf{X}_A)$ adequately represents all of the contributions introduced by the *entire* laser optical system, including those from the collimation and time delay optics. This approximation is reasonable because most of the aberration originates in or around the large aperture amplifiers, where the small field angles associated with the large beamwidth are more susceptible to perturbations by the optics and air paths. Phase perturbations beyond the collimators will be less effective in producing speckle at the focusing lenses because the field angles are larger and the remaining propagation distances are smaller; thus the simulations presented here will slightly overestimate the structure.

We calculate the beam propagation using the Huygens-Fresnel integral.[20] In the scaled

coordinates $\mathbf{X}_A \equiv \mathbf{x}_A/D_A$ and $\mathbf{X}_C \equiv \mathbf{x}_C/D_C$, the converging phase curvature imposed by the weak focusing optic at $A$ is $-\pi |D_A\mathbf{X}_A|^2/(\lambda f_A)$, while the diverging curvature imposed by the collimator $C$ is $+\pi |D_C\mathbf{X}_C|^2/(\lambda |f_C|)$. The focal lengths $f_A$ and $f_C$ are related to the propagation distance $z_{AC}$ and geometrical optics beamwidths by

$$|f_C|/f_A = D_C/D_A, \quad |f_C| + z_{AC} = f_A.$$

In the paraxial approximation, the collimated beam amplitude just beyond $C$ is then

$$
\begin{aligned}
E_C(\mathbf{X}_C) &= \frac{D_A^2}{\lambda z_{AC}} \exp\left(i\pi\frac{|D_C\mathbf{X}_C|^2}{\lambda|f_C|}\right) \int E_A'(\mathbf{X}_A) \exp\left(-i\pi\frac{|D_A\mathbf{X}_A|^2}{\lambda f_A}\right) \\
&\quad \times \exp\left(\frac{i\pi}{\lambda z_{AC}}|D_C\mathbf{X}_C - D_A\mathbf{X}_A|^2\right) d^2\mathbf{X}_A \\
&= \frac{1}{M_{AC}Z_{AC}} \int E_A'(\mathbf{X}_A) \exp\left(\frac{i\pi}{Z_{AC}}|\mathbf{X}_C - \mathbf{X}_A|^2\right) d^2\mathbf{X}_A,
\end{aligned}
\tag{6}
$$

where $M_{AC} = D_C/D_A = |f_C|/f_A$ is the spatial magnification (now $< 1$) and $Z_{AC} \equiv \lambda z_{AC}/(D_A D_C) \ll 1$ is the propagation distance $z_{AC}$ scaled to the Fresnel length $D_A D_C/\lambda$. Similarly, the amplitude just before the final focusing lens $L$ at distance $z_{CL}$ is given by

$$E_L(\mathbf{X}_L) = \frac{1}{Z_{CL}} \int E_C(\mathbf{X}_C) \exp\left(\frac{i\pi}{Z_{CL}}|\mathbf{X}_L - \mathbf{X}_C|^2\right) d^2\mathbf{X}_C,$$

where $\mathbf{X}_L \equiv \mathbf{x}_L/D_L = \mathbf{x}_L/D_C$ and $Z_{CL} \equiv \lambda z_{CL}/(D_C D_L) \equiv \lambda z_{CL}/D_C^2$ $(M_{CL} \to 1)$. We can also relate $E_L$ directly to $E_A'$ by combining these expressions and integrating over $\mathbf{X}_C$:

$$E_L(\mathbf{X}_L) = \frac{1}{M_{AC}Z_{AL}} \int E_A'(\mathbf{X}_A) \exp\left(\frac{i\pi}{Z_{AL}}|\mathbf{X}_L - \mathbf{X}_A|^2\right) d^2\mathbf{X}_A,
\tag{7}$$

where $Z_{AL} \equiv Z_{AC} + Z_{CL}$. Because these expressions have the same form, one can describe all the quasi near-field propagation simply by summing the appropriate dimensionless path-lengths $Z_{AC}$, $Z_{CL}$, etc, even if the beam expands or converges along the path.

The final lens provides the phase curvature $-\pi \left| D_L \mathbf{X}_L \right|^2 / \left( \lambda f_L \right)$ required to focus $E_L$ to its far-field amplitude $E_F$. Substituting $E_L' \left( \mathbf{X}_L \right) \equiv E_L \left( \mathbf{X}_L \right) \exp \left[ -i\pi \left| D_L \mathbf{X}_L \right|^2 / \left( \lambda f_L \right) \right]$ into the Huygens-Fresnel integral for a distance equal to the focal length $f_L$, we obtain

$$E_F \left( \mathbf{X}_F \right) = \left( 1/F_L \right) \exp \left( i\pi F_L \left| \mathbf{X}_F \right|^2 \right) \mathfrak{F} \left[ E_L, -\mathbf{X}_F \right] , \tag{8}$$

where $\mathbf{X}_F \equiv \mathbf{x}_F / d_F$ is scaled to the diffraction-limited width $d_F \equiv f_L \lambda / D_L$ and $F_L \equiv \lambda f_L / D_L^2$. As in the near-field case, we can write $E_F$ directly in terms of $E_A'$ by substituting (7) and integrating over $\mathbf{X}_L$:

$$E_F \left( \mathbf{X}_F \right) = \left( 1/M_{AC} F_L \right) \exp \left[ i\pi \left( F_L - Z_{AL} \right) \left| \mathbf{X}_F \right|^2 \right] \mathfrak{F} \left( E_A', -\mathbf{X}_F \right) . \tag{9}$$

This recovers the well-known result that the far-field amplitude differs from the exact Fourier transform of the aperture amplitude only by a phase curvature term, which does not affect the focal intensity distribution $I_F \left( \mathbf{X}_F, t \right) = \left| E_F \left( \mathbf{X}_F \right) \right|^2$.

The above expressions can be evaluated numerically by FFT methods. For example, FFT calculates the far-field $E_F \left( \mathbf{X}_F \right)$ directly from Eqs. (8) or (9). In principle one can also use FFT to evaluate $E_L \left( \mathbf{X}_L \right)$ directly by expressing the integral in (7) as $\mathfrak{F} \left( E_A'', -\mathbf{X}_L / Z_{AL} \right)$, where $E_A'' \left( \mathbf{X}_A \right) \equiv E_A' \left( \mathbf{X}_A \right) \exp \left[ i\pi \left( \left| \mathbf{X}_A \right|^2 + \left| \mathbf{X}_L \right|^2 \right) / Z_{AL} \right]$; however that approach is not well suited to the near-field regime because the small values of $Z_{AL}$ introduce rapid phase oscillations in $E_A'' \left( \mathbf{X}_A \right)$. Instead, we use (7) to relate the Fourier-transformed amplitudes $\tilde{E}_L \left( \boldsymbol{\beta} \right) \equiv \mathfrak{F} \left( E_L, -\boldsymbol{\beta} \right)$ and $\tilde{E}_A' \left( \boldsymbol{\beta} \right) \equiv \mathfrak{F} \left( E_A', -\boldsymbol{\beta} \right)$ by a unitary propagator; i.e.,

$$\tilde{E}_L \left( \boldsymbol{\beta} \right) = \left( M_{AC} \right)^{-1} \tilde{E}_A' \left( \boldsymbol{\beta} \right) \exp \left( -i\pi Z_{AL} \left| \boldsymbol{\beta} \right|^2 \right) \tag{10}$$

The inverse transform $E_L \left( \mathbf{X}_L \right) \equiv \mathfrak{F} \left( \tilde{E}_L, +\mathbf{X}_L \right)$ then yields the desired amplitude, which gives the speckle intensity $I_L \left( \mathbf{X}_L, t \right) = \left| E_L \left( \mathbf{X}_L \right) \right|^2$.

The time-averaged ISI propagation can always be simulated by superimposing the random speckle patterns calculated from a large ensemble of statistically-independent realizations of the complex object amplitude $E_O(\mathbf{x})$. In each realization, $E_O(\mathbf{x})$ is modelled by a 2D circular array of random complex numbers satisfying Gaussian statistics with equal RMS values. This produces a "top-hat" *average* intensity distribution imbedded in an otherwise empty square window to provide guard bands. For each realization, one would use the FFT to calculate the exit pupil amplitude $E'_A(\mathbf{X}_A)$ from Eqs. (4) and (5), assuming a uniform intensity transmission $|T(\mathbf{X}_A)| = 1$ in a square aperture and a random phase aberration $\phi(\mathbf{X}_A)$ of specified RMS amplitude and gradient. (This aperture is also imbedded in a larger window to provide guard bands.) To allow for overfilling at the aperture, one must choose the number of points across the object to be somewhat larger than the width (in XDL units) of the desired beam profile at the target. The far-field and quasi near-field intensity profiles are then evaluated using the formulas derived above. Although this approach is straightforward, the large number of realizations required to adequately smooth out the statistical nonuniformities leads to excessive calculation times, even for moderately structured beams.

In the simulations presented here, we use a faster alternative approach that relates the average intensity profile (i.e., the intensity envelope) directly to the spatial autocorrelation function just after the exit pupil at $A$:

$$\Gamma'_A(\mathbf{X}_A, \mathbf{X}'_A) \equiv \langle E'_A(\mathbf{X}_A) E'^*_A(\mathbf{X}'_A) \rangle = T_A(\mathbf{X}_A) T^*_A(\mathbf{X}'_A) \Gamma_A(\mathbf{X}_A, \mathbf{X}'_A), \qquad (11)$$

where $\langle \rangle$ denotes an ensemble-average. The incident correlation function $\Gamma_A(\mathbf{X}_A, \mathbf{X}'_A) \equiv \langle E_A(\mathbf{X}_A) E^*_A(\mathbf{X}'_A) \rangle$ is related to the correlation function $\Gamma_O(\mathbf{X}_O, \mathbf{X}'_O) \equiv \langle E_O(\mathbf{X}_O) E^*_O(\mathbf{X}'_O) \rangle$

11

at the object plane by expression (5):

$$\Gamma_A \left( \mathbf{X}_A, \mathbf{X}'_A \right) = F_A^2 \int \int \Gamma_O \left( \mathbf{X}_O, \mathbf{X}'_O \right) \exp \left[ -i2\pi \left( \mathbf{X}_A \cdot \mathbf{X}_O - \mathbf{X}'_A \cdot \mathbf{X}'_O \right) \right] d^2 \mathbf{X}_O d^2 \mathbf{X}'_O .$$

Because average intensity nonuniformities are lumped into $\left| T_A \left( \mathbf{X}_A \right) \right|^2$ instead of $\Gamma_A \left( \mathbf{X}_A, \mathbf{X}_A \right)$, we can write $\Gamma_A \left( \mathbf{X}_A, \mathbf{X}'_A \right) \simeq \Gamma_A \left( \mathbf{X}_A - \mathbf{X}'_A \right)$. One can model this condition and still allow a nonuniform object intensity envelope $\langle I_O \left( \mathbf{X}_O \right) \rangle$ by adopting the incoherent approximation $\Gamma_O \left( \mathbf{X}_O, \mathbf{X}'_O \right) \simeq \langle I_O \left( \mathbf{X}_O \right) \rangle \delta \left( \mathbf{X}_O - \mathbf{X}'_O \right)$ , thereby giving the Van Cittert-Zernike result [11]

$$\Gamma_A \left( \mathbf{X}_A - \mathbf{X}'_A \right) = F_A^2 \, \mathfrak{F} \left[ \langle I_O \rangle , - \left( \mathbf{X}_A - \mathbf{X}'_A \right) \right] . \tag{12}$$

We now construct a numerical algorithm based on FFT techniques that directly evaluates the envelope profile $\langle I \left( \mathbf{X} \right) \rangle = \left\langle \left| E \left( \mathbf{X} \right) \right|^2 \right\rangle$ at either the focal spot $\left[ \langle I \left( \mathbf{X} \right) \rangle \rightarrow \langle I_F \left( \mathbf{X}_F \right) \rangle \right]$ or the quasi near-field [e.g., $\langle I \left( \mathbf{X} \right) \rangle \rightarrow \langle I_L \left( \mathbf{X}_L \right) \rangle$] by modifying a well-known formalism used to describe partially-coherent images.[11],[14] Combining expression (11) with either (9) or (7), then substituting (12) we can write the general result

$$
\begin{aligned}
\langle I \left( \mathbf{X} \right) \rangle &= \int \int \Gamma_A \left( \mathbf{X}_A, \mathbf{X}'_A \right) T_A \left( \mathbf{X}_A \right) K \left( \mathbf{X}, \mathbf{X}_A \right) T_A^* \left( \mathbf{X}'_A \right) K^* \left( \mathbf{X}, \mathbf{X}'_A \right) d^2 \mathbf{X}_A d^2 \mathbf{X}'_A \\
&= \int \langle I_O \left( \mathbf{X}_O \right) \rangle \left| F_A \int T_A \left( \mathbf{X}_A \right) K \left( \mathbf{X}, \mathbf{X}_A \right) \exp \left( -i2\pi \mathbf{X}_A \cdot \mathbf{X}_O \right) d^2 \mathbf{X}_A \right|^2 d^2 \mathbf{X}_O , \quad (13)
\end{aligned}
$$

where the respective far-field and near-field kernels $K \rightarrow K_{F,L}$ are:

$$K_F \left( \mathbf{X}_F, \mathbf{X}_A \right) \equiv \left( M_{AC} F_L \right)^{-1} \exp \left( -i2\pi \mathbf{X}_F \cdot \mathbf{X}_A \right) \tag{14}$$

$$K_L \left( \mathbf{X}_L, \mathbf{X}_A \right) \equiv \left( M_{AC} Z_{AL} \right)^{-1} \exp \left( i\pi Z_{AL}^{-1} \left| \mathbf{X}_L - \mathbf{X}_A \right|^2 \right) . \tag{15}$$

With these kernels, expression (13) reduces to

$$\langle I_F \left( \mathbf{X}_F \right) \rangle = \int \langle I_O \left( \mathbf{X}_O \right) \rangle S_F \left( \mathbf{X}_F + \mathbf{X}_O \right) d^2 \mathbf{X}_O \tag{16}$$

$$\langle I_L \left( \mathbf{X}_L \right) \rangle = \int \langle I_O \left( \mathbf{X}_O \right) \rangle S_L \left( \mathbf{X}_L + Z_{AL} \mathbf{X}_O \right) d^2 \mathbf{X}_O , \tag{17}$$

where the point-spread functions are

$$S_F\left(\mathbf{X}\right) \;\equiv\; \left|\left(C/F_L\right)\mathfrak{F}\left(T_A, -\mathbf{X}\right)\right|^2 \tag{18}$$

$$S_L\left(\mathbf{X}\right) \;\equiv\; \left|\frac{C}{Z_{AL}}\int T_A\left(\mathbf{X}_A\right)\exp\left(\frac{i\pi}{Z_{AL}}\left|\mathbf{X}-\mathbf{X}_A\right|^2\right)d^2\mathbf{X}_A\right|^2 \tag{19}$$

and $C \equiv F_A/M_{AC}$. Equation (16) is the well-known convolution that relates the focal image profile to the incoherent object and a point-spread function $S_F\left(\mathbf{X}\right)$ dominated by the phase aberration in $T_A\left(\mathbf{X}_A\right)$. As long as $S_F\left(\mathbf{X}\right)$ remains narrow compared to $\langle I_O\left(\mathbf{X}_O\right)\rangle$, its detailed shape and structure will have little effect on $\langle I_F\left(\mathbf{X}_F\right)\rangle$, except for some rounding near the edges. This is illustrated in Fig. 3, which simulates ISI on the Nike laser under typical operating conditions. The near-field result (17) is equivalent to the convolution used to describe Fresnel diffractive effects in radiography,[15] but its point-spread function (19) has now been generalized to include phase aberration. Expression (17) is dominated by the structure in $S_L\left(\mathbf{X}\right)$ when $Z_{AL}\max\left(\mathbf{X}_O\right) \ll \max\left(\mathbf{X}_L\right)$; it begins to smooth out only when $Z_{AL}\max\left(\mathbf{X}_O\right)$ becomes comparable to $\max\left(\mathbf{X}_L\right)$. (As expected, (17) approaches the far-field shape $\langle I_F\rangle$ in the Fraunhofer limit $Z_{AL}\to\infty$.)

The integrals in (18) and 19 are identical to those of the respective far-field and near-field amplitudes (9) and (7), except for replacing $E'_A\left(\mathbf{X}_A\right)$ by $T_A\left(\mathbf{X}_A\right)$. Their evaluation therefore follows the same steps as those for the amplitudes; i.e., $S_F\left(\mathbf{X}\right)$ is found by applying the FFT directly to expression (18), but $S_L\left(\mathbf{X}\right)$ requires that we express $T_A\left(\mathbf{X}_A\right)$ in terms of its Fourier transform $\tilde{T}_A\left(\boldsymbol{\beta}\right) \equiv \mathfrak{F}\left(T_A, -\boldsymbol{\beta}\right)$ before integrating (19) to obtain

$$S_L\left(\mathbf{X}\right) = \left|C\int \tilde{T}_L\left(\boldsymbol{\beta}\right)\exp\left(i2\pi\mathbf{X}\cdot\boldsymbol{\beta}\right)d^2\boldsymbol{\beta}\right|^2 = \left|C\,\mathfrak{F}\left(\tilde{T}_L,\mathbf{X}\right)\right|^2, \tag{20}$$

where $\tilde{T}_L\left(\boldsymbol{\beta}\right) \equiv \tilde{T}_A\left(\boldsymbol{\beta}\right)\exp\left(-i\pi Z_{AL}\left|\boldsymbol{\beta}\right|^2\right)$ is calculated from the same unitary propagator

used for the complex amplitudes in Eq. (10).

Expressions (16) and 17 can be efficiently solved numerically by taking the Fourier transforms $\left\langle \tilde{I}\left(\boldsymbol{\beta}\right)\right\rangle \equiv \mathfrak{F}\left(\left\langle I\right\rangle, -\boldsymbol{\beta}\right)$, applying the convolution theorem[11], and recalling (12):

$$\left\langle \tilde{I}_F\left(\boldsymbol{\beta}\right)\right\rangle = \mathfrak{F}\left(\left\langle I_O\right\rangle, +\boldsymbol{\beta}\right)\mathfrak{F}\left(S_F, -\boldsymbol{\beta}\right) = F_A^{-2}\Gamma_A\left(-\boldsymbol{\beta}\right)\ \mathfrak{F}\left(S_F, -\boldsymbol{\beta}\right) \tag{21}$$

$$\left\langle \tilde{I}_L\left(\boldsymbol{\beta}\right)\right\rangle = \mathfrak{F}\left(\left\langle I_O\right\rangle, +Z_{AL}\boldsymbol{\beta}\right)\mathfrak{F}\left(S_L, -\boldsymbol{\beta}\right) = F_A^{-2}\Gamma_A\left(-Z_{AL}\boldsymbol{\beta}\right)\ \mathfrak{F}\left(S_L, -\boldsymbol{\beta}\right) \tag{22}$$

The envelopes then follow from the inverse transforms $\langle I_{F,L}\left(\mathbf{X}_{F,L}\right)\rangle = \mathfrak{F}\left(\tilde{I}_{F,L}, +\mathbf{X}_{F,L}\right)$.

Figure 4 compares the envelope profiles with the intensities averaged over 8000 statistical realizations at both the near- and far-field planes. Even with the reduced widths and structure in these simulations (e.g., 32 XDL instead of 75 XDL), the averaging approach required several hours, whereas the direct envelope calculations took less than 30 seconds. This large difference in running times and the excellent agreement at all locations confirm the value of the new algorithm. Except for the residual Fresnel diffraction spikes at the edges, the envelope structure at the focusing lens arises entirely from phase aberration; when this aberration is switched off, only the Fresnel spikes remain.

The above analysis was carried out for the Nike baseline case shown in Fig. 2, where a diverging mirror collimates the beam before it focuses, but it can apply equally well to the alternative case where a converging mirror collimates the beam after it traverses a focus. (See Fig. 10) This option would require the output beams to be enclosed in an evacuated tunnel, which would probably be desirable in any case to avoid excessive phase distortion from air turbulence or nonlinear optical effects in the long demultiplexing paths. To treat this configuration, the above formalism requires only two modifications: (a) change the sign of the scaled propagation distance $Z_{AC}$, and (b) invert all profiles at and beyond the

14

collimators [e.g., $\langle I_C\left(\mathbf{X}_L\right)\rangle \rightarrow \langle I_C\left(-\mathbf{X}_L\right)\rangle$].

## Results and Discussion

In this section, we compare ISI average intensity simulations with measured quasi near-field speckle on the Nike laser, compare the ISI speckle with that of spatially-coherent light, and explore options for reducing the structure. (Detailed comparisons of Nike far-field profiles are described in refs. [7] and [10].) The simulations use the same parameters as in Fig. 3; i.e., a "top-hat" object profile of diameter $N_F = 75$ XDL, a uniformly illuminated square amplifier aperture of width $D_A = 60$ cm, and random-phase aberration of $\lambda/4$ rms amplitude characterized by a point-spread function of $\sim 15$ XDL half-energy width. In all cases, the collimated beamwidths are $D_C = 15$ cm and the aperture-collimator distances are $z_{AC} = 53$ m, thus giving the scaled $A$-$C$ distance $Z_{AC} = \lambda z_{AC}/\left(D_A D_C\right) = 1.46 \times 10^{-4}$.

Using a setup similar to that described in ref. [12], we recorded time-integrated near-field images of several Nike beams on photochromic UV-sensitive PERM film (manufactured by GAF Chemicals).[21] For each beam, we measured the image at both the collimator and the target chamber window during the same laser shot by placing film over one half of the recollimator and allowing the unblocked half of the beam to propagate on to the window. (See Fig. 2.) The windows are located one meter beyond the 6 meter focusing lenses, so the geometrical beamwidths at the windows are $D_W = 5/6 D_C = 12.5$ cm. To avoid saturating the film, we fired the system only up to the 20 cm driver amplifier, but not the 60 cm final stage. This does not affect the measurements because the quasi near-field structure is dominated by imperfections in the final amplifier optics, and does not depend on laser intensity. The film was digitized using a commercial 8-bit scanner (HP ScanJet IIc). We

15

calibrated the film response at 248 nm by using repeated shots from a small KrF laser to vary the total film exposure from 1 to 50 mJ/cm$^2$, thus creating a custom greyscale target. A scan of this target revealed that its weak saturation behavior was well approximated by an exponential function, which was then used to linearize the raw image data.

Figure 5 shows the recorded ISI images and lineouts at the recollimator mirror array and target chamber windows, while Fig. 6 shows the corresponding simulations. (In these and in all other near-field lineouts, the fluences are normalized to the average value across the geometrical optics beamwidth between $-0.5$ and $+0.5$.) The measured fluences in Fig. 5 lie well within the linear portion of the PERM film response, with average intensities $\sim 5$ mJ/cm$^2$. Beam #38 (Figs. 5b and 6b) has one of the shorter collimated propagation paths, with a total collimator-focusing lens distance $z_{CL} = 41$ meters and a scaled distance $Z_{CL} = \lambda z_{CL}/D_C^2 = 4.52 \times 10^{-4}$; beam #10 (Figs. 5c and 6c) has one of the longer paths, with a total distance $z_{CL} = 76$ meters and $Z_{CL} = \lambda z_{CL}/D_C^2 = 8.38 \times 10^{-4}$. Because the aperture-recollimator distance is nearly the same for all beams, we show the recollimator results only for beam #10. Figures 5 and 6 clearly show that the structure becomes coarser as the light propagates farther from the amplifier aperture, as expected from Eq. (17). Figure 6 also indicates that the nonuniformity amplitudes increase at first, then saturate and slowly decrease as the pathlength increases.

Figure 7 compares the RMS transverse mode amplitudes corresponding to the structure shown in Figs. 5 and 6. To obtain these spectra, we used a procedure similar to that of ref. [10]; i.e., we averaged the 1D FFT power spectra over a large number of horizontal lineouts, then took the square root. For the simulated data, the lineouts included the entire beams;

for the measured data, we averaged over 150 lines, excluding those in the weaker portions of the beams and those containing the anomalously large hot spot at the top center of the image in Fig. 5b. To avoid spurious contributions due to rapid rolloff at the edges of the beams, we applied a 1D Hanning window[22] to the data. (This affects only the first nonzero mode.) The RMS amplitudes are scaled to the zeroth component, and the mode numbers correspond to the number of cycles across the geometrical optics beamwidth.

Figures 7b,c show good agreement between the measured and simulated data except for the broadband shelf above 20 cycles, which appears to be film noise. A comparison between Figs. 7b and 7c also shows the spectral narrowing due to the suppression of higher spatial frequencies in the longer propagation path of beam #10, as noted above. Figure 7a shows generally lower amplitudes at the recollimators, as clearly seen in Fig. 6, but the measured beam profile contains additional higher spatial frequency structure not present in the simulated profile. This structure, which also shows up as the weak semicircular rings and radial striations in Fig. 5a, appears to be caused by HR optical coating imperfections in a large circular mirror located between the 20cm and 60cm amplifiers. Because it occurs predominantly at spatial frequencies above those in the simulated image, it tends to diffract away more effectively with increasing propagation distance, and thus has little impact on the results shown in Figs. 7b,c.

Figure 8 shows the simulated structure in beam #10 for the case of spatially-coherent light. This corresponds to a point source object $\langle I_O (\mathbf{X}_O) \rangle \rightarrow \delta (\mathbf{X}_O)$, so $\langle I_L (\mathbf{X}_L) \rangle$ in Eq. (17) reduces to the usual Fresnel diffraction result (19). Comparing Fig. 8 with the ISI case in Figs. 6a and 6c, we see that the structure is nearly the same at the recollimator, with only

a small enhancement of the Fresnel spikes at the edges. As the propagation path increases, however, the structure becomes far more severe than that of the ISI case, with hot-spots as large as 10 times the average fluence. The difference occurs because ISI filtered out more of the high spatial frequency components with increasing propagation path. This can be easily explained by using either Eq. (17) or the alternative ISI model mentioned above, in which the object encodes itself into small independent coherence zones of width $d_A = D_A/N_F$ at the amplifier aperture. ($N_F = 75$ XDL in these simulations) Because ISI averages out interference from aperture points separated by more than $d_A$, it effectively cuts off all of the structure with transverse wavelengths shorter than some minimum value $\Lambda$. To estimate $\Lambda$ at the collimator, we note that according to Eq. (6), any two aperture points $\mathbf{X}_A$ and $\mathbf{X}'_A$ separated by scaled distance $d_A/D_A$ will produce an interference pattern of scaled minimum wavelength $\Lambda_C/D_C = N_F Z_{AC}$; a similar argument applied to Eq. (7) gives the analogous result $\Lambda_F/D_F = N_F Z_{AL} = N_F (Z_{AC} + Z_{CL})$ at the lens. Recalling the definitions of $Z_{AC}$ and $Z_{CL}$, we then obtain $\Lambda_C/D_C \simeq 1/91.3$ and $\Lambda_F/D_F \simeq 1/13.6$, which is consistent with Fig. 8. At the collimator, ISI allows components with up to 91 cycles across the beamwidth, so it reduces only the sharp Fresnel spikes at the edges; at the lens, however, ISI allows fewer than 14 cycles, so it suppresses almost all of the sharp high spatial frequency structure. The ISI filtering process is less effective in beam #38, allowing up to 22 cycles across the beam at the lens plane ($\Lambda_F/D_F \simeq 1/22.3$). This contrast is also evident in Fig. 7.

One obvious way of reducing the quasi near-field structure is to reduce the phase aberration, as illustrated in Fig. 9. Comparing Figs. 9 and 6a,b, we see that a $\sim 2\text{-}fold$ reduction in point-spread width would also reduce the nonuniformities by $\sim 2\text{-}fold$. A reduction of

this magnitude should be possible in future KrF drivers, which would use evacuated beam paths and take advantage of ion milling techniques to improve optical surface quality. It is also highly desirable for achieving better control over the far-field profile by minimizing the blurring effects due to phase aberration.

The structure can also be reduced by using optical relaying, which can be readily implemented by the configuration shown in Fig. 10. Here one replaces the diverging collimator of Fig. 2 by a converging mirror located a distance equal to its focal length $f_C > 0$ beyond the beam focus, thus giving an aperture-collimator separation distance $z_{AC} = f_A + f_C$. The scaled distance now reverses sign to become $Z_{AC} \rightarrow -\lambda z_{AC}/(D_A D_C)$, but because its magnitude is the same as in the previous configuration, the structure at the collimator remains qualitatively similar to that of Fig. 6a. In this configuration, an image $I_1$ of the amplifier aperture forms at a distance $z_{CI} = z_{AC} D_C/D_A = 13.25$ m beyond the collimator. (This follows from the requirement that the scaled propagation distance vanishes: $Z_{AI} \equiv Z_{AC} + Z_{CI} = -\lambda z_{AC}/(D_A D_C) + \lambda z_{CI}/D_C^2 = 0$.) At plane $R_1$ located a distance $z_{CI}$ beyond $I_1$, the scaled propagation distance increases to $Z_{CI} = |Z_{AC}|$, so the transverse fluence distribution becomes an exact inverted image of Fig. 6a. The amplitude of the structure begins to increase beyond $R_1$, so that would be the last chance to place the first optic of a 1 : 1 image relay telescope without subjecting it to larger fluence spikes. The structure at the second optic $R_2$ (at a distance $2z_{CI}$ from $R_1$) is comparable to that of $R_1$, and the telescope creates a second image plane $I_2$ at a distance $4z_{CI} = 53$ m from the first one. Because the final focusing lens $L$ could be safely placed an additional distance of only $z_{CI}$ beyond this image, the largest total available delay time beyond $I_1$ is $5z_{CI}/c = 221$ ns.

This would be insufficient for some of the beams in a large angularly-multiplexed system, so these beams would require an additional relay telescope.

In principle, it would also be possible to reduce the structure by taking advantage of the ISI filtering process discussed above. In an angularly-multiplexed system, however, that approach would require long propagation paths to the time demultiplexing mirrors, as well as to the focusing lenses. It would result in excessively long propagation paths for all the beams, which could, in turn, make beam alignment more difficult and create possible imprinting problems at the far-field.

<center>Summary and Conclusion</center>

Although ISI provides ultrasmooth illumination at the far-field of a laser, it still allows speckle to develop in the quasi near-field beams. This paper has compared simulations of that speckle with measurements in the output beams of the Nike laser and explored options for controlling the problem in future KrF drivers. The speckle arises from phase aberration in the system, and builds up as the beams propagate away from the exit pupil plane at the final amplifier. Because of the spatial incoherence of ISI light, the speckle is significantly smaller than that developed by coherent light; nevertheless, it remains a damage issue for the higher fluences and long delay paths required in future angularly-multiplexed KrF drivers.

We have examined two techniques for calculating the average intensities. The first propagates a randomly-selected stochastic optical field amplitude through the laser system to evaluate the instantaneous intensity, then repeats this procedure with multiple new statistical realizations to accumulate the time-average intensity. The second, which is much faster,

evaluates the ensemble-average intensity envelope directly using FFT and a correlation function algorithm. Benchmark tests show excellent agreement (within $< 1\%$ rms) between the two approaches, providing confidence that the algorithm can be routinely applied to calculations and analysis.

The Nike simulations, which are in good qualitative agreement with the photochromic film measurements, show that as the distance from the amplifier increases, (a) the structure becomes coarser and (b) the hot-spot amplitudes increase at first, then appear to saturate and slowly decrease. We also performed simulations to explore options for reducing the near-field structure in future KrF drivers. One possibility is to reduce the phase aberration; e.g., a 2-$fold$ reduction in point-spread width would also reduce the amplitudes by $\sim$ 2-$fold$. The second option uses optical relaying, but that would probably be expensive to implement in some of the longer beam paths required for demultiplexing.

## Appendix

This appendix examines the condition necessary to satisfy the quasi-monochromatic approximation. The basic criterion requires the optical bandwidth $\Delta\nu$ to be narrow enough that it does not suppress interference structure in the propagation. To get interference at point $\mathbf{X}_L$ between light originating from the two aperture points $\mathbf{X}_A$ and $\mathbf{X}'_A$ (e.g., see Fig. 2), the total path difference between the two rays must be smaller than the coherence length $c\tau_c \simeq c/\Delta\nu \sim 300~\mu$m for $\Delta\nu \sim 1$ THz. In the paraxial approximation, the pathlength for a

single ray is the total phase shift divided by $k_0 \equiv 2\pi/\lambda$:

$$l\left(\mathbf{X}_A, \mathbf{X}_L\right) \simeq z_{AC} + z_{CL} + (2\pi/\lambda)^{-1}\left(\pi/Z_{AL}\right)\left|\mathbf{X}_L - \mathbf{X}_A\right|^2, \qquad \text{(A1)}$$

where the transverse contribution $\left(\pi/Z_{AL}\right)\left|\mathbf{X}_L - \mathbf{X}_A\right|^2$ comes from expression (7). (As expected, the minimum value of $l\left(\mathbf{X}_A, \mathbf{X}_L\right)$ occurs for rays that satisfy the geometrical optics condition $\mathbf{X}_L = \mathbf{X}_A$.) The criterion $\left|l\left(\mathbf{X}_A, \mathbf{X}_L\right) - l\left(\mathbf{X}'_A, \mathbf{X}_L\right)\right| < c/\Delta\nu$ then becomes

$$Z_{AL}^{-1}\left|\left|\mathbf{X}_L - \mathbf{X}_A\right|^2 - \left|\mathbf{X}_L - \mathbf{X}'_A\right|^2\right| < 2\nu_0/\Delta\nu, \qquad \text{(A2)}$$

where $\nu_0 = c/\lambda \sim 1200$ THz. For *spatially*-coherent light the largest factor in (A2) would occur, for example, when $\mathbf{X}'_A = -\mathbf{X}_A = \mathbf{X}_L$ and $|\mathbf{X}_L| = 1/\sqrt{2}$; the criterion then reduces to $Z_{AL} > \Delta\nu/\nu_0 \sim 8\times10^{-4}$. In Figure 8, this is marginally satisfied at the target chamber, where $Z_{AL} = Z_{AC} + Z_{CL} = 9.84\times10^{-4}$, but not at the recollimator, where $Z_{AL} \to Z_{AC} = 1.46\times10^{-4}$. Thus the very high spatial frequency ringing shown at the recollimator in Fig. 8 (i.e., the fine Fresnel structure at the edges) would actually be washed out at the bandwidths of interest. For ISI light of far-field XDL width $N_F$, the factors in (A2) would be limited by the diameter $1/N_F \ll 1$ of the spatial coherence zones; hence the criterion becomes

$$Z_{AL} > (2N_F)^{-2}\,\Delta\nu/\nu_0; \qquad \text{(A3)}$$

which is easily satisfied even at the recollimators when $N_F = 75$ XDL.

[1] M. H. Emery, J. H. Gardner, R. H. Lehmberg, and S. P. Obenschain, "Hydrodynamic target response to an induced spatial incoherence-smoothed laser beam," Phys. Fluids B **3**, 2640-2650 (1991)

[2] J. D. Kilkenny, S. G. Glendinning, S. W. Haan, B. A. Hammel, J. D. Lindl, D. Munro, B. A. Remington, S. V. Weber, J. P. Knauer and C. P. Verdon, "A review of the ablative stabilization of the Rayleigh-Taylor instability in regimes relevant to inertial confinement fusion," Phys. Plasmas **1**, 1379-1389 (1994)

[3] R. H. Lehmberg and S. P. Obenschain,"Use of induced spatial incoherence for uniform illumination of laser fusion targets," Optics Comm. **46**, 27-31 (1983); R. H. Lehmberg, A. J. Schmitt, and S. E. Bodner, "Theory of induced spatial incoherence," J. Appl. Phys. **62**, 2680-2701 (1987)

[4] R. H. Lehmberg and J. Goldhar, "Use of incoherence to produce to produce smooth and controllable irradiation profiles with KrF fusion lasers," Fusion Technol. **11**, 532-541 (1987)

[5] J. M. D. Lister, M. J. Shaw, C. J. Hooker, and E. C. Harvey, "Uniform target illumination by induced spatial incoherence in a multiplexed KrF laser system," Optics Comm. **84**, 55-60 (1991)

[6] R. H. Lehmberg, S. P. Obenschain, C. J. Pawley, M. S. Pronko, A. V. Deniz, and T. Lehecka, "Effects of random phase distortion and nonlinear optical processes on laser

beam uniformity and spatial incoherence (ISI)," in *Laser coherence control: technology and applications*, H. T. Powell and T. Kessler, eds., Proc. SPIE **1870**, 163-174 (1993)

[7] T. Lehecka, R. H. Lehmberg, A. V. Deniz, K. A. Gerber, S. P. Obenschain, C. J. Pawley, M. S. Pronko and C. A. Sullivan, "Production of high energy uniform focal profiles with the Nike laser," Optics Comm. **117**, 485-491 (1995)

[8] S. P. Obenschain, et. al., "The Nike laser facility: Performance and initial target experiments," Phys. Plasmas **3**, 2098-2107 (1996)

[9] C. J. Pawley, et. al., "Measurements of laser-imprinted perturbations and Rayleigh-Taylor growth with the Nike laser," Phys. Plasmas **4**, 1969-1977 (1997)

[10] A. V. Deniz, T. Lehecka, R. H. Lehmberg and S. P. Obenschain, "Comparison between measured and calculated nonuniformities of Nike laser beams smoothed by induced spatial incoherence," Optics Comm. **147**, 402-410 (1998)

[11] J. W. Goodman, *Statistical Optics* (John Wiley & Sons, New York, 1985)

[12] J. D. Sethian, et. al., "Large area electron beam pumped krypton fluoride laser amplifier," Rev. Sci. Instrum. **68**, 2357-2366 (1997)

[13] M. W. McGeoch, P. A. Corcoran, R. G. Altes, I. D. Smith, S. E. Bodner, R. H. Lehmberg, S. P. Obenschain, and J. D. Sethian, "Conceptual design of a 2-MJ KrF laser fusion facility," Fusion Technol. **32**, 610-643 (1997)

[14] B. J. Thompson, "Image formation with partially coherent light," in *Progress in Optics*, E. Wolf, Ed., **7**, 169-191 (North Holland Publishing Company, Amsterdam, 1969)

[15] W. H. Steel, M. De, and J. A. Bell, "Diffraction Corrections in Radiometry," J. Opt. Soc. Am. **62**, 1099-1103 (1972)

[16] S. Skupsky, R. W. Short, T. Kessler, R. S. Craxton, S. Letzring and J. M. Soures, "Improved laser-beam uniformity using the angular dispersion of frequency-modulated light," J. Appl. Phys. **66**, 3456-3462 (1989); S. Skupsky and R. S. Craxton, "Irradiation uniformity for high-compression laser-fusion experiments," Phys. Plasmas **6**, 2157-2163 (1999)

[17] S. P. Regan, et. al., "Experimental investigation of smoothing by spectral dispersion," J. Opt. Soc. Am. B **17**, 1483-1489 (2000)

[18] D. Véron, A. Ayral, C. Gouédard, D. Husson, J. Lauriou, O. Martin, B. Meyer, M. Rostaing and C. Sauteret, "Optical spatial smoothing of Nd-Glass laser beam," Optics Comm. **65**, 42-46 (1988); D. Véron, G. Thiell and C. Gouédard, "Optical smoothing of the high power PHEBUS Nd-glass laser using the multimode optical fiber technique," Optics Comm. **97**, 259-271 (1993)

[19] H. Nakano, K. Tsubakimoto, N. Miyanaga, M. Nakatsuka, T. Kanabe, H. Azechi, T. Jitsuno and S. Nakei, "Spectrally dispersed amplified spontaneous emission for improving irradiation uniformity into high power Nd:glass laser system," J. Appl. Phys. **73**, 2122-2131 (1993)

[20] J. W. Goodman, *Introduction to Fourier Optics*, 2nd ed. (McGraw-Hill, New York, 1996)

[21] D. F. Lewis, "A processless film for recording electron beam radiation," Proc. SPIE **1079**, 162-169 (1989)

[22] W. H. Press, B. P. Flannery, S. A. Teukolsky and W. T. Vetterling, *Numerical Recipes; the Art of Scientific Computing*, (Cambridge University Press, New York, 1988)
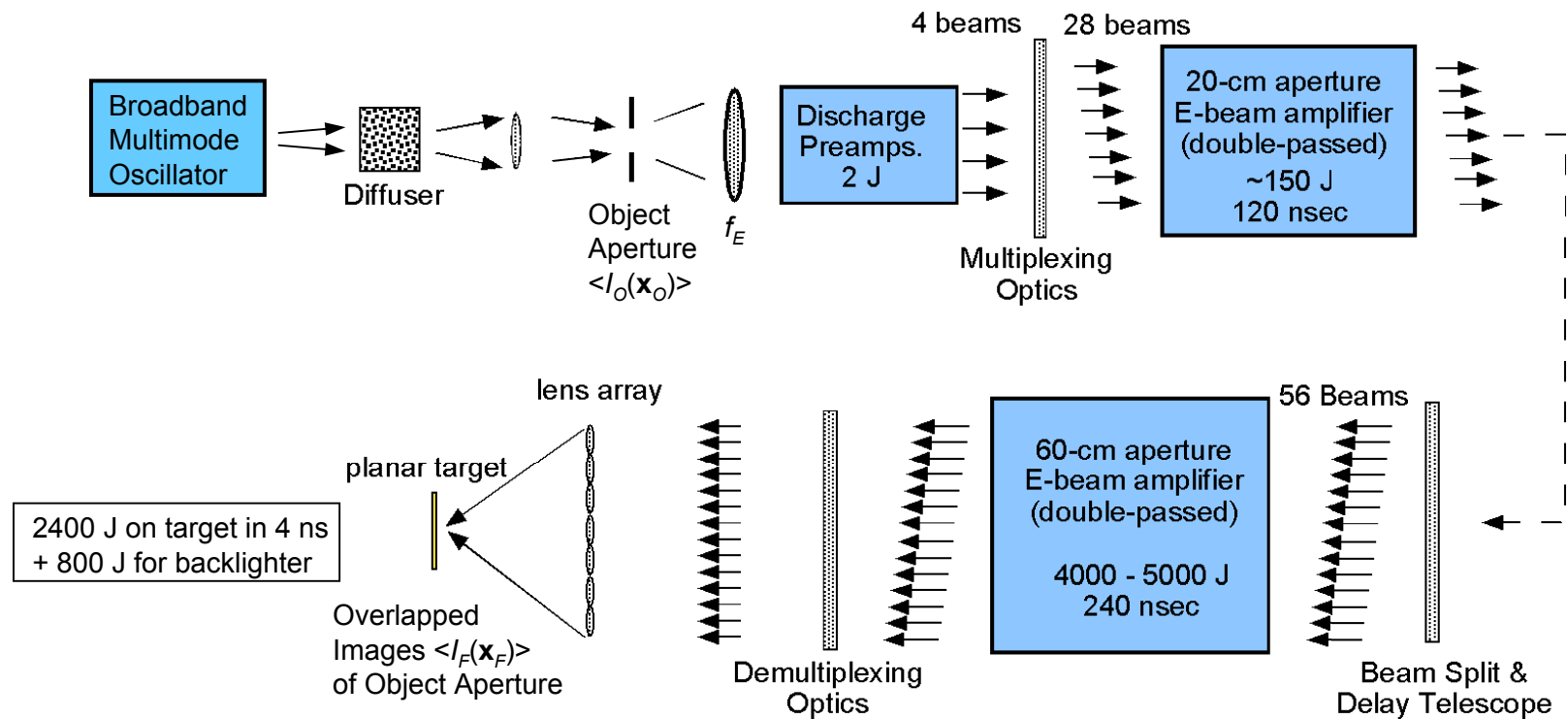
Fig. 1. Nike amplifier staging and angularly multiplexed optical system. The object aperture is uniformly illuminated by spatially and temporally incoherent light, then imaged onto the target through the amplifier system. The beams overlap at the amplifiers, which are placed at or near images of the object's Fourier-transform (pupil) plane.

Fig. 2. Schematic of one beam of the Nike optical system starting at the 60 cm amplifier (aperture stop A), converging to the recollimating mirror C, then propagating along delay path $z_{CL} = z_{CM} + z_{ML}$ to focusing lens L. The wavy line at A represents the random phase of complex transmission $T_A(\mathbf{x})$. The amplifier is double-passed, so the large lens represents a concave mirror. The dotted lines near C and L illustrate the placement of the film packs where the beam #10 profiles were measured.

Fig. 3. Simulations of the point-spread function and ISI focal profile on the Nike laser, assuming a 75 XDL wide "top-hat" object profile, a uniformly illuminated 60 cm amplifier, and random-phase aberration of $\lambda/4$ rms amplitude and $\sim 15$ XDL point-spread width.

Fig. 4. Comparison of ISI far-field and near-field intensities averaged over 8000 coherence times (thin lines) with envelope intensities (heavy lines). In these simulations, the object fluence is a 32 XDL wide "top-hat" profile and the random-phase aberration is modelled by a $\sim 7$ XDL point-spread width.

Fig. 5. Photochromatic film images and calibrated lineouts at the Nike laser recollimator mirror array and target chamber windows: (a) Beam #10 at the recollimator mirror and (b), (c) Beams #38 and #10, respectively, at the target chamber.

Fig. 6. Simulations of ISI intensity envelope images and lineouts at the Nike laser recollimator array and target chamber windows: (a) Beam #10 (or #38) at the recollimator mirror and (b), (c) Beams #38 and #10, respectively, at the target chamber.

Fig. 7. 1D mode spectra of measured (——) and simulated (- - - -) near-field fluence structure at the Nike laser recollimator array and target chamber windows: (a) Beam #10 recollimator mirror and (b), (c) Beams #38 and #10, respectively, at the target chamber. The measured data has larger statistical variations because it averages over fewer horizontal lines.

Fig. 8. Simulations of coherent intensity images and lineouts at the recollimator mirror and target chamber window of Nike beam #10. (Note the extended ordinate scale in the lineouts, compared to the earlier figures.)

Fig. 9. Same as Fig. 6a,b, except that the point-spread width is 8 XDL instead of 15 XDL

Fig. 10. Schematic of an alternate ISI optical system at and beyond the final aperture stop A, showing the beam focusing before the recollimating mirror C, propagating through the first amplifier image plane $I_1$ to a 1 : 1 relay telescope beginning at $R_1$, and producing a second amplifier image plane $I_2$ before the final focusing lens.

Fig. 1: Nike amplifier staging and angularly multiplexed optical system. The object aperture is uniformly illuminated by spatially and temporally incoherent light, then imaged onto the target through the amplifier system. The beams overlap at the amplifiers, which are placed at or near images of the object's Fourier-transform (pupil) plane.
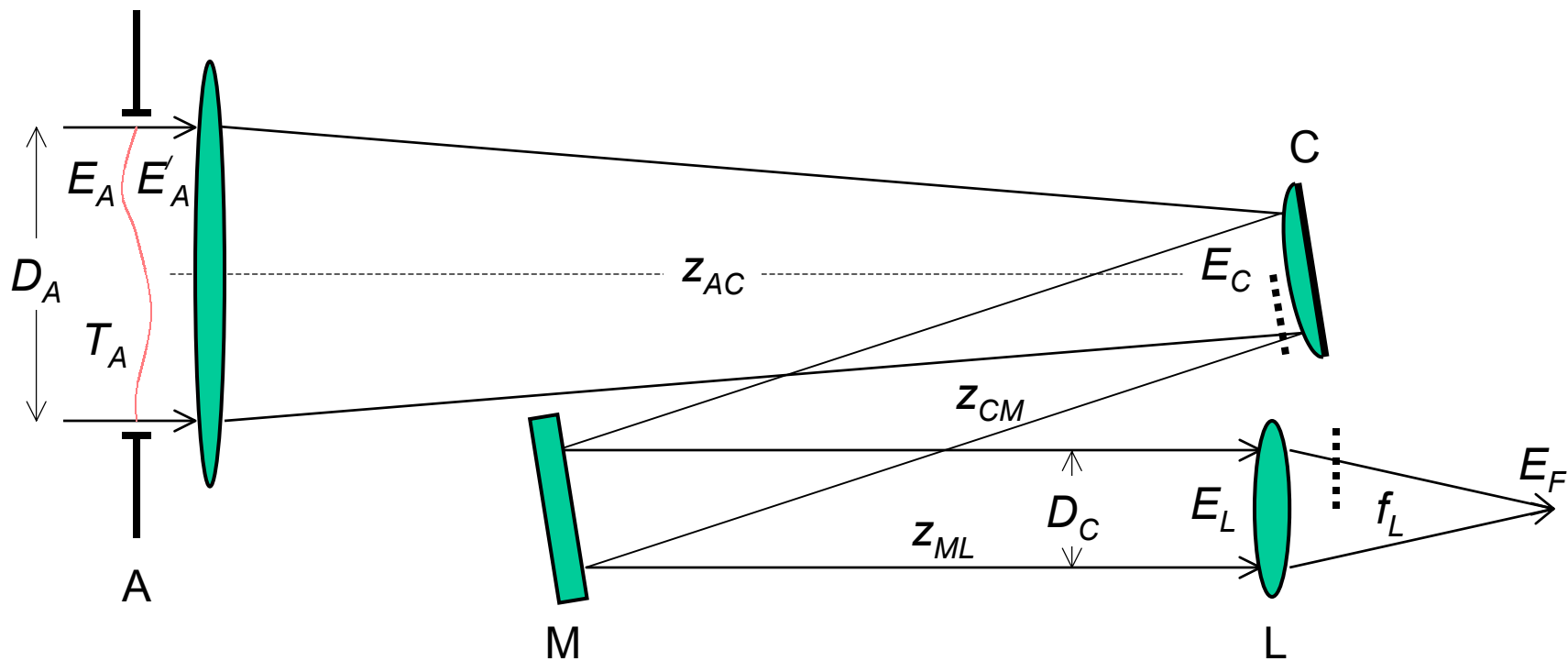
Fig. 2: Schematic of one beam of the Nike optical system starting at the 60 cm amplifier (aperture stop A), converging to the recollimating mirror C, then propagating along delay path $z_{CL} = z_{CM} + z_{ML}$ to focusing lens L. The wavy line at A represents the random phase of complex transmission $T_A(\mathbf{x})$. The amplifier is double-passed, so the large lens represents a concave mirror. The dotted lines near C and L illustrate the placement of the film packs where the beam profiles were measured.
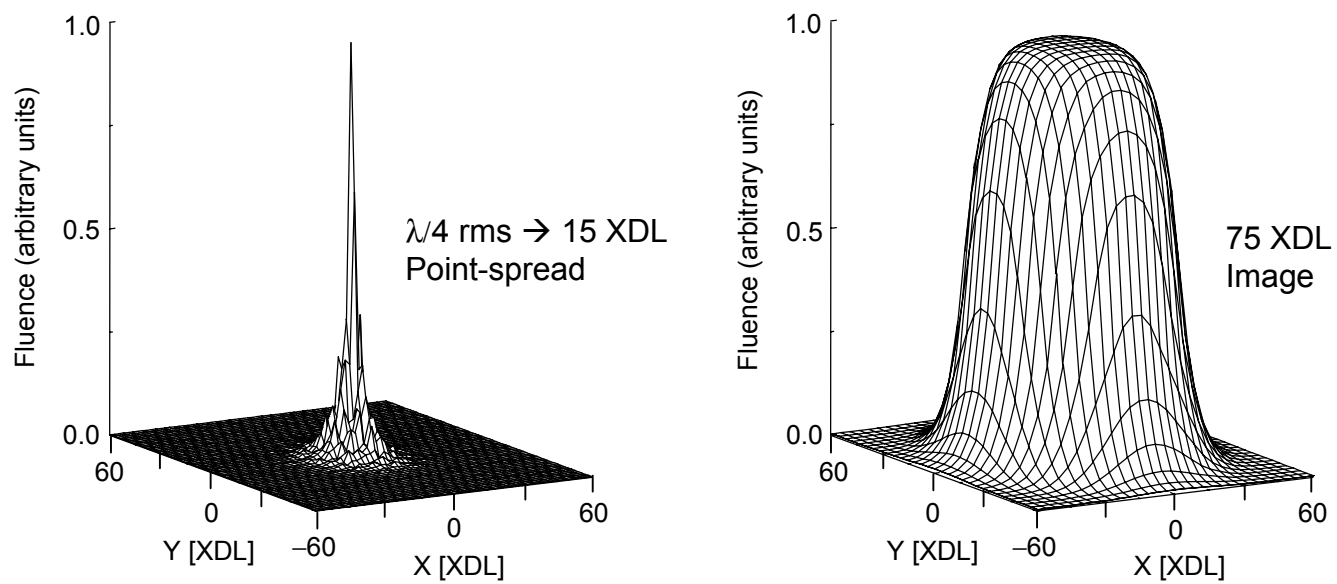
Fig. 3. Simulations of ISI on the Nike laser with a 75 XDL wide "top hat" object profile, uniformly illuminated 60 cm amplifier, and random-phase aberration of λ/4 rms amplitude giving a point-spread function of ~15 XDL width.
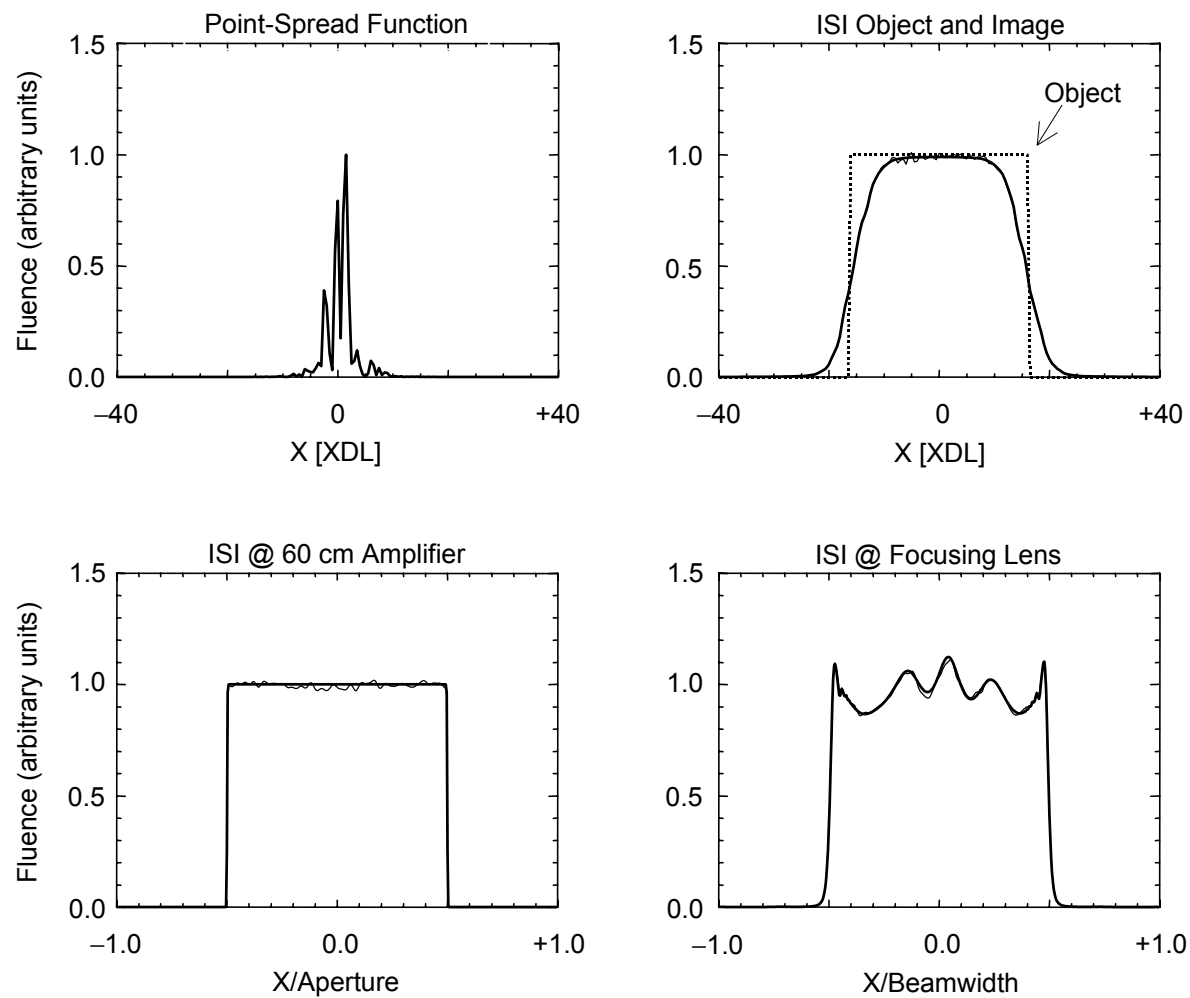
Fig. 4.  Comparison of ISI intensities averaged over 8000 coherence times (thin lines) with envelope intensities (heavy lines) at the far-field, the laser aperture, and final focusing lens. In these simulations, the object fluence is a 32 XDL wide "top-hat" profile and the random-phase aberration is modelled by a ~7 XDL point-spread width.

Fig. 5. Photochromatic film images and calibrated lineouts at the Nike laser recollimator mirror array and target chamber windows: (a) Beam #10 at the recollimator mirror and (b), (c) Beams #38 and #10, respectively, at the target chamber.

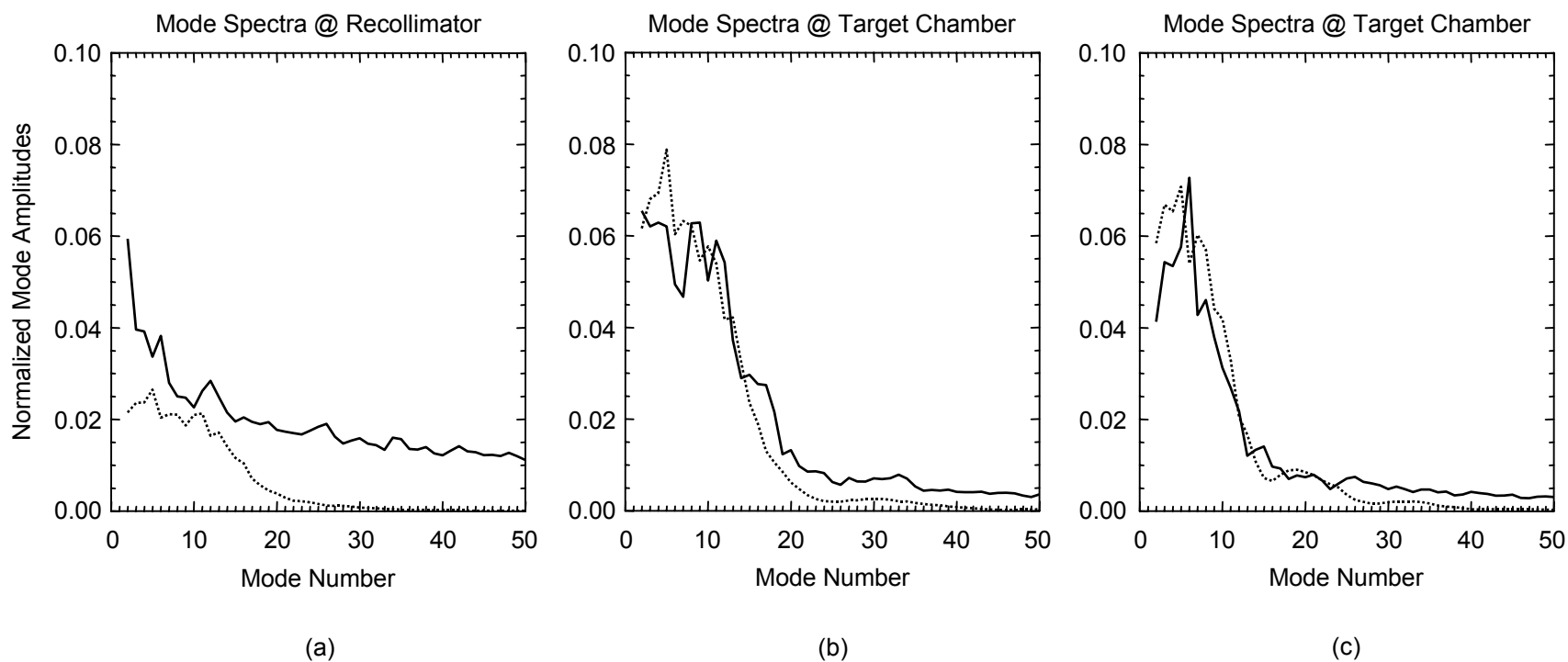Fig. 6. Simulations of ISI intensity envelope images and lineouts at the Nike laser recollimator array and target chamber windows: (a) Beam #10 (or #38) at the recollimator mirror and (b), (c) Beams #38 and #10, respectively, at the target chamber.

Fig. 7. 1D mode spectra of measured (——) and simulated (- - - -) near-field fluence structure at the Nike laser recollimator array and target chamber windows: (a) Beam #10 recollimator mirror and (b), (c)  Beams #38 and #10, respectively, at the target chamber. The measured data has a larger statistical variations because it averages over fewer horizontal lines.
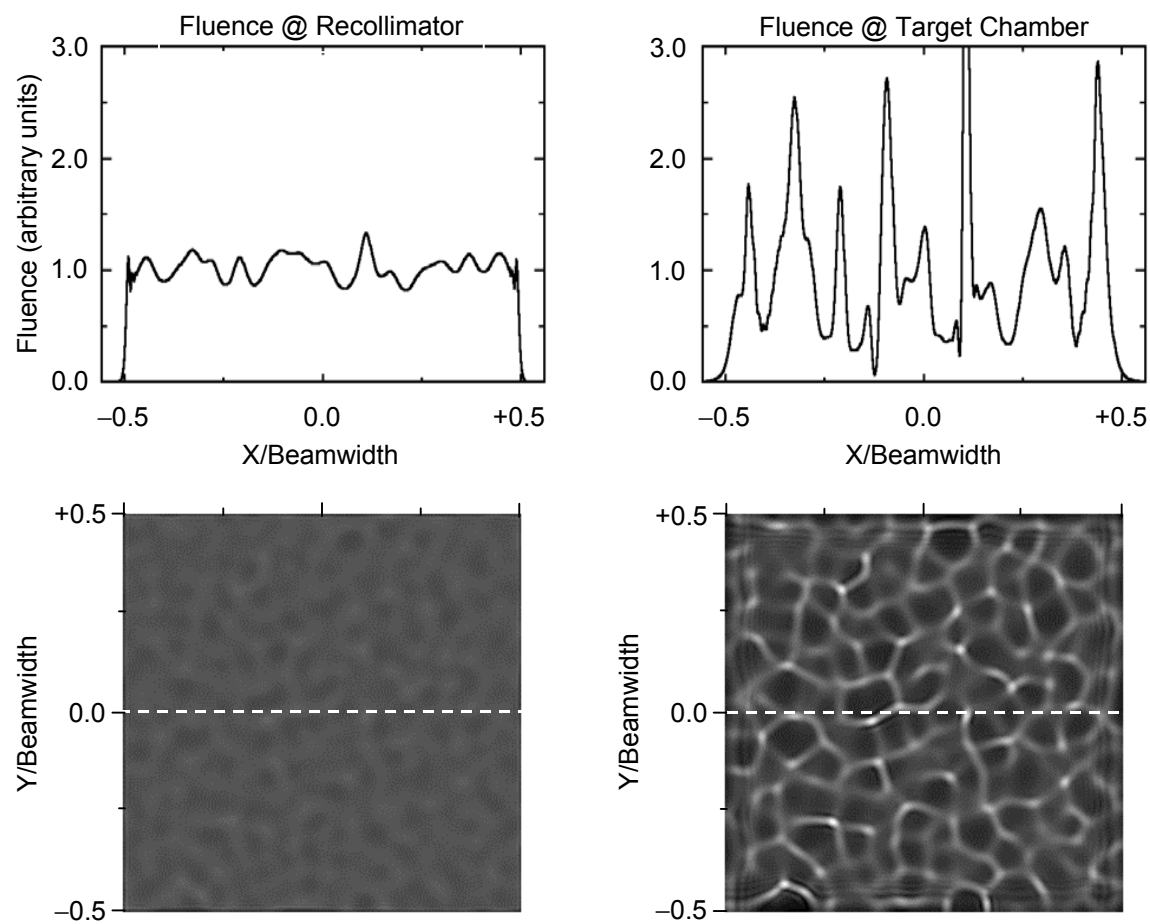
Fig. 8. Simulations of coherent intensity images and lineouts at the recollimator mirror and target chamber window of Nike beam #10. (Note the extended ordinate scale in the lineouts, compared to the earlier figures.)
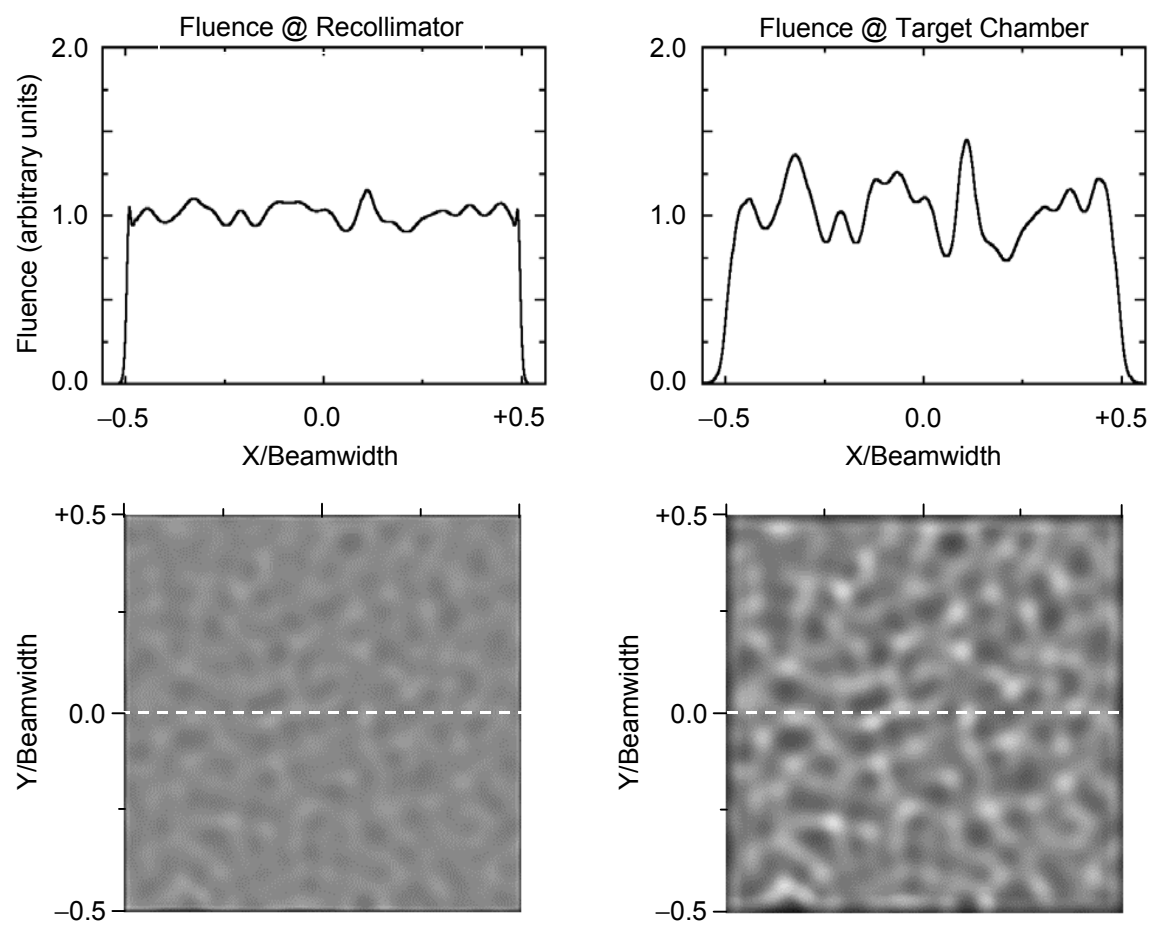
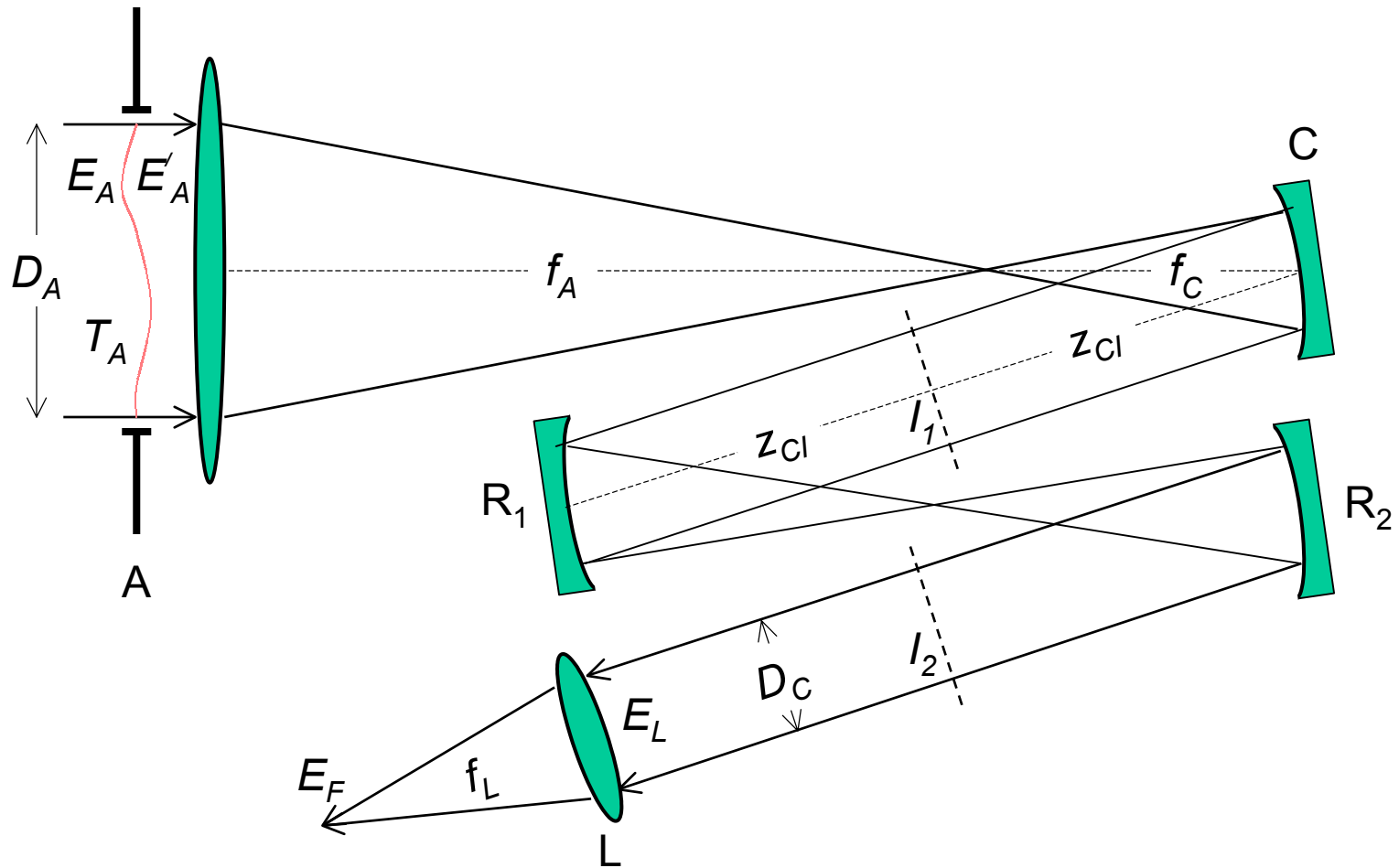Fig. 9. Same as Fig. 6a,b, except that the point-spread width is 8 XDL instead of 15 XDL

Fig. 10. Schematic of an alternate ISI optical system at and beyond the final aperture stop A, showing the beam focusing before the recollimating mirror C, propagating through the first amplifier image plane $I_1$ to a 1 : 1 relay telescope beginning at $R_1$, and producing a second amplifier image plane $I_2$ before the final focusing lens.